OEA | Opto-Electronic Advances

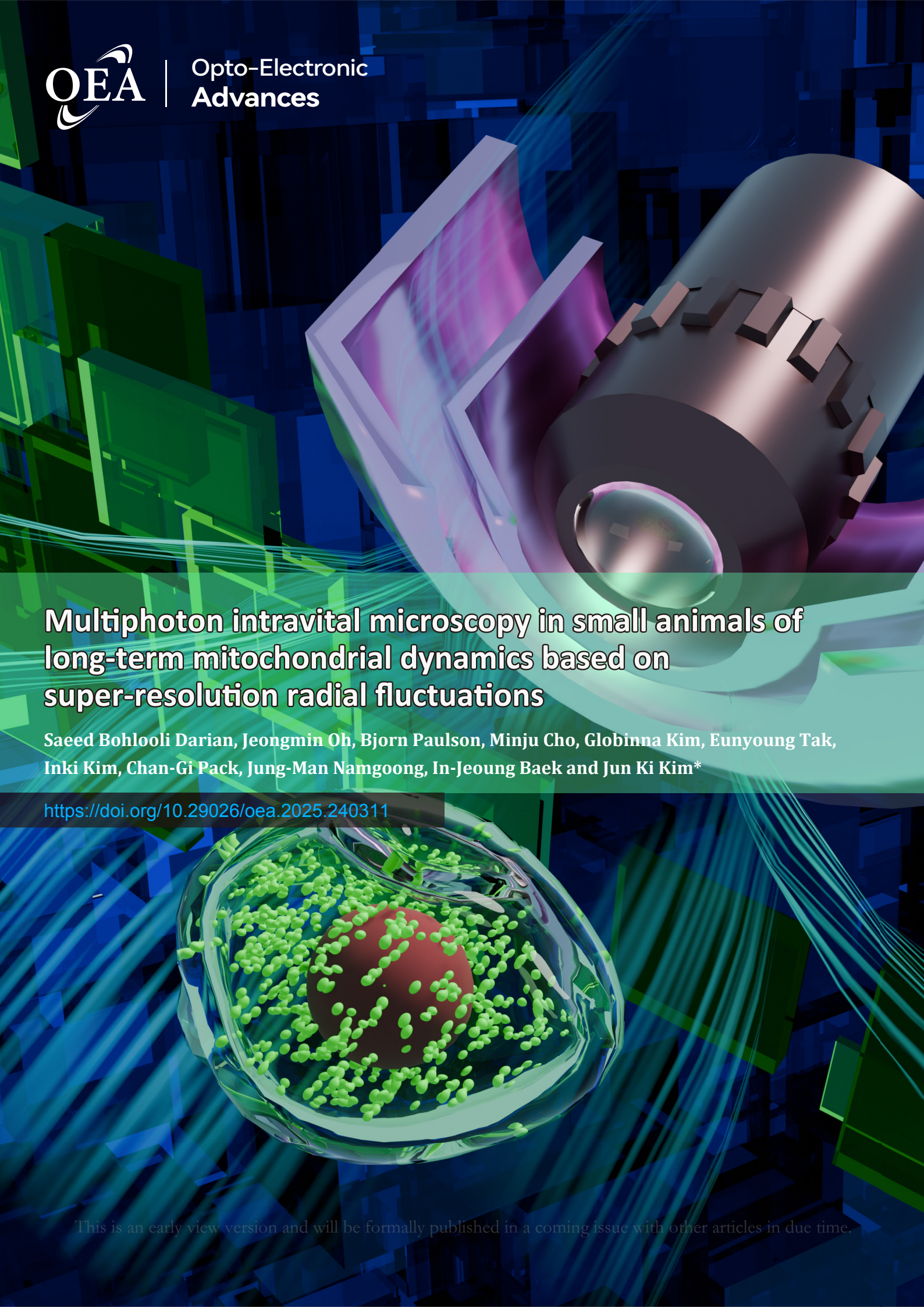

Multiphoton intravital microscopy in small animals of long-term mitochondrial dynamics based on super-resolution radial fluctuations

Saeed Bohlooli Darian, Jeongmin Oh, Bjorn Paulson, Minju Cho, Globinna Kim, Eunyoung Tak, Inki Kim, Chan-Gi Pack, Jung-Man Namgoong, In-Jeoung Baek and Jun Ki Kim*

https://doi.org/10.29026/oea.2025.240311

Opto-Electronic Advances

CN 51–1781/TN ISSN 2096–4579 (Print) ISSN 2097–3993 (Online)

Multiphoton intravital microscopy in small animals of long-term mitochondrial dynamics based on superresolution radial fluctuations

Saeed Bohlooli Darian, Jeongmin Oh, Bjorn Paulson, Minju Cho, Globinna Kim, Eunyoung Tak, Inki Kim, Chan-Gi Pack, Jung-Man Namgoong, In-Jeoung Baek and Jun Ki Kim

Citation: Darian SB, Oh J, Paulson B, et al. Multiphoton intravital microscopy in small animals of long-term mitochondrial dynamics based on superresolution radial fluctuations. *Opto-Electron Adv* **8**, 240311(2025).

https://doi.org/10.29026/oea.2025.240311

Received: 23 December 2024; Accepted: 21 April 2025; Published online: 11 June 2025

Opto-Electronic Advances

Article

July 2025, Vol. 8, No. 7

DOI: 10.29026/oea.2025.240311 CSTR: 32247.14.oea.2025.240311

Multiphoton intravital microscopy in small animals of long-term mitochondrial dynamics based on super-resolution radial fluctuations

Saeed Bohlooli Darian[1], Jeongmin Oh[2], Bjorn Paulson[2], Minju Cho[1], Globinna Kim[1], Eunyoung Tak[1,2], Inki Kim[3], Chan-Gi Pack[1,2], Jung-Man Namgoong[4], In-Jeoung Baek[1,2] and Jun Ki Kim[1,2]*

We developed an imaging technique combining two-photon computed super-resolution microscopy and suction-based stabilization to achieve the resolution of the single-cell level and organelles *in vivo*. To accomplish this, a conventional two-photon microscope was equipped with a 3D-printed holders, which stabilize the tissue surface within the focal plane of immersion objectives. Further computational image stabilization and noise reduction were applied, followed by super-resolution radial fluctuations (SRRF) analysis, doubling image resolution, and enhancing signal-to-noise ratios for *in vivo* subcellular process investigation. Stabilization of < 1 μm was obtained by suction, and < 25 nm were achieved by subsequent algorithmic image stabilization. A Mito-Dendra2 mouse model, expressing green fluorescent protein (GFP) in mitochondria, demonstrated the potential of long-term intravital subcellular imaging. *In vivo* mitochondrial fission and fusion, mitochondrial status migration, and the effects of alcohol consumption (modeled as an alcoholic liver disease) and berberine treatment on hepatocyte mitochondrial dynamics are directly observed intravitally. Suction-based stabilization in two-photon intravital imaging, coupled with computational super-resolution holds promise for advancing *in vivo* subcellular imaging studies.

Keywords: SRRF; in vivo subcellular imaging; mitochondiral dynamics; multiphoton intravital microscopy; super resolution radial fluctuations

Darian SB, Oh J, Paulson B et al. Multiphoton intravital microscopy in small animals of long-term mitochondrial dynamics based on super-resolution radial fluctuations. *Opto-Electron Adv* **8**, 240311 (2025).

Introduction

Intravital microscopy is a transformative technology in biological sciences, enabling high-resolution imaging of cells and tissues within living organisms. It provides unique insights into cellular interactions in native microenvironments. Initially developed in the 19th century with brightfield transillumination for studying blood flow[1,2]. Intravital microscopy has since evolved with advancements, such as confocal microscopy, structured illumination[3], and multiphoton microscopy[4,5]. These techniques enhance imaging depth and detail, capturing

[1]Department of Biomedical Engineering, Brain Korea 21 Project, University of Ulsan College of Medicine, Seoul 05505, Republic of Korea; [2]Convergence Medicine, Asan Institute for Life Sciences, Asan Medical Center, Seoul 05505, Republic of Korea; [3]Department of Pharmacology, University of Ulsan College of Medicine, Seoul 05505, Republic of Korea; [4]Department of Surgery, Asan Medical Center, University of Ulsan College of Medicine, Seoul 05505, Republic of Korea.

*Correspondence: JK Kim, E-mail: kim@amc.seoul.kr

Received: 23 December 2024; Accepted: 21 April 2025; Published online: 11 June 2025

dynamic physical and chemical interactions critical for understanding diseases and therapeutic responses.

Multiphoton microscopy, with its nonlinear optical excitation, achieves deeper tissue penetration and reduced photodamage compared to confocal microscopy. By utilizing nonlinear optical excitation[6], and longer wavelengths[7], multiphoton systems minimize photodamage, photobleaching, and scattering, enabling visualization of tissue layers inaccessible to standard techniques. Furthermore, advancements such as large-field objective lenses enhance imaging capabilities and provide more comprehensive and detailed imaging results[8]. However, challenges persist, such as resolving structures smaller than half the wavelength of light due to the optical diffraction limit. Super-resolution techniques, such as structured illumination, PALM, STORM, mSTED, and optical fluctuation imaging[9–11] address these limitations but are hindered by specific fluorophore requirements, photobleaching, and limited penetration depth.

A computational super-resolution technique, called super-resolution radial fluctuations (SRRF)[12–14], overcomes many limitations of traditional methods. SRRF does not depend on convergence in a modern machine-learning, as it does not involve a loss function to minimize or gradient descent optimization. Instead, the algorithm calculates the degree to which intensity distributions resemble a radial symmetry about each pixel (or sub-pixel when a magnification factor is applied) in the image. SRRF enhances resolution and reduces noise by leveraging the temporal correlation of radial symmetry fluctuations, eliminating the need for iterative optimization. Convergence is ensured by assuming each fluorophore generates a symmetric fluctuation pattern around its true position.

The SRRF algorithm is compatible with standard wide-field microscopes and itself has been validated for microscopy data several times in the literature. It has been successfully applied in cellular imaging[15], DNA measurement[16], calcium imaging[17], microvascular ultrasound imaging[18], and traction force microscopy[19]. Its accessibility makes it a promising tool for advancing live imaging.

Physiological motion from sources like respiration, heartbeat, and blood flow presents significant challenges to intravital imaging, often causing image instability. To address these issues, stabilization strategies are categorized as active, passive, pharmaceutical, and algorithmic approaches[20–22]. Active stabilization methods leverage technologies such as piezoelectric controllers[23] and contact sensors[24], use real-time feedback to counteract motion to enable rapid physical actuation[23]. However, these methods often require hardware modifications to the microscope[25], and demand precise, rapid actuation, limiting their accessibility and versatility.

Passive approaches include mechanical pressure, ultrafast imaging, and time-gated synchronization with physiological cycles. While mechanical pressure stabilizes tissue, it risks impairing blood flow and biological relevance[26], whereas ultrafast imaging is constrained to single-shot scenarios[27]. Time-gated imaging offers improved stability[28] but is invasive and technically demanding. Tissue clamps, although effective, are unsuitable for delicate systems[29]. Pharmaceutical strategies aim to reduce motion with drugs[30] but risk altering cellular pathways and are insufficient for organs with high intrinsic motion, like the heart or lungs, where displacements can range from a hundred of microns to 0.5 cm in a single cycle[31].

A promising passive strategy is suction-based stabilization[29,32–34], which uses negative pressure to minimize tissue displacement without disrupting organ functionality or blood flow. This minimally invasive[35] technique maintains a stable imaging plane, prevents cell damage, and allows repositioning during imaging. Suction stabilization has been particularly effective in dynamic organs like the lungs and heart, and thorax in mouse models[29,32–34,36], enabling high-resolution, motion artifact-free intravital imaging across various biological systems. Additionally, if any movement was detected within the field of view, an autocorrelation-based drift correction was applied within the SRRF algorithm to ensure accurate image reconstruction.

Mitochondria, essential for energy production and cellular adaptation, play a critical role in various cellular functions, encompassing energy production, and maintaining blood-brain barrier integrity. Their dynamics, governed by fusion and fission processes, facilitate the exchange of solutes, metabolites, and proteins[37]. Fusion process[38,39] is mediated by Mitofusin 1/2 (outer membrane) and optic atrophy 1 (inner membrane), while fission involves endoplasmic reticulum interactions at mitochondrial DNA-marked constriction sites[40].

Mitochondrial dysfunction contributes to metabolic disorders like obesity[41], insulin resistance[42], and diabetes[43]. However, imaging their structure and dynamics *in vivo* remains challenging due to technical limitations,

including insufficient resolution of confocal and multi-photon microscopes, as mitochondrial size in humans range from 0.5 to 10 μm in size[44], and tissue movement artifacts. These obstacles hinder research into mitochondrial functions and the development of targeted therapies. For example, ethanol-induced oxidative stress[45] affects mitochondria in alcoholic liver injury[46,47], while Berberine (BBR)[48], a bioactive compound, disrupts mitochondrial function by inhibiting respiratory complex I, leading to oxidative stress and apoptosis[49]. BBR is also being explored as a potential inhibitor of mitochondrial fission.

We developed a novel super-resolution intravital imaging technique combining two-photon microscopy, suction-based tissue stabilization, and SRRF post-processing algorithm. This enabled subcellular imaging of fluorescent mitochondria in single hepatocytes at nanometer-scale resolution. A 3D-printed holder provided suction-induced stabilization, allowing high NA objective lenses for prolonged imaging while maintaining blood flow. The system reduced tissue movement and radial fluctuations for over 30 minutes.

We validated the method by imaging mitochondrial fission and fusion in Mito-dendra2 fluorescent mice and observed subcellular changes in models of alcoholic liver injury and BBR treatment. This approach provides a powerful tool for studying mitochondrial dynamics and cellular homeostasis *in vivo*, offering insights into metabolic and mitochondrial disorders. It holds potential for advancing therapeutic strategies and elucidating biological mechanisms in animal models.

Methods

Animal experiments

All animal experiments followed the guidelines of the Korean Ministry of Food and Drug Safety under the Laboratory Animal Act and were approved by the Institutional Animal Care and Use Committee of the Asan Institute for Life Sciences (permit number: 2021-12-030). Transgenic mitochondria dendra2 green fluorescent protein mice (#018397, Jackson Laboratory, USA) were used and maintained in a local colony.

Mice were housed in groups of five at 23 °C with ad libitum access to food and water under a 12 hour dark/light cycle. Anesthesia was induced in 25–35 g male and female mice via intraperitoneal injection of a zoletil, rompun, and PBS mixture (6:4:90, 10 mL/kg). During procedures, mice were placed on a heated stage at 37 °C, intubated, and ventilated (harvard apparatus miniVent 845) during imaging. Additional anesthetic was administered as needed to prevent movement.

For intravital imaging, an abdominal incision was made to expose the liver and for surface observation. For lung and heart imaging, a chest incision was created and held open with a retractor until the stabilization holder was inserted. Breathing rate and body temperature were continuously monitored, with similar surgical techniques applied to other organs as needed.

Imaging

We utilized a two-photon imaging system (IVM-MS, IVIM Technology) with a Ti:Sapphire laser (Coherent Inc.) at 920 nm to capture high-resolution *in vivo* mitochondrial images. The microscope is compatible with SHG, CFP, GFP, RFP, and Cy5 channels, and required no modifications to the existing microscope setup. Imaging was performed using either an oil-immersion objective (1.45 NA, 100×, Olympus) or a water-immersion objective (1.1 NA, 25×, Nikon) for optimal resolution.

Stabilizer design and implementation

Custom suction-based holders were designed in SolidWorks and 3D-printed to facilitate intravital imaging. The holder features a single-chamber suction stabilizer with a hollow wall that transfers negative pressure from an external pump to the sample surface. It is adaptable to various objective lenses, reducing costs and design efforts, while minimizing *z*-axis drift through short imaging intervals. The base is sealed with 3 mm or 8 mm coverslips for vacuum stabilization and compatibility with oil and water immersion objectives under index-matching conditions. Vacuum was maintained via a 3 mm conduit connected to a pump with a regulator, liquid absorber, and pressure valve to optimize suction while avoiding immersion material interference.

Vacuum stabilization allowed reproducible control of object movement, critical for imaging modalities. Serially mounted vacuum regulators managed suction pressure, with adjustments for planar and angular positioning achieved using a microstage with six degrees of freedom. Negative pressure levels, ranging from 25–75 mmHg, were selected based on the holder's geometry, target, and animal blood pressure to ensure adequate contact without damaging the tissue.

Sterile PBS was applied periodically to maintain tissue

hydration during imaging. The stabilizer ensured sufficient adhesion without compressing or impairing organ motion, allowing unobstructed blood circulation within the imaging window.

Image analysis

The images were processed using Fiji 1.54 software[50]. Regions of interest were delineated to measure mean fluorescence signals, and mitochondrial signals were isolated by thresholding to remove background fluorescence. Background noise was reduced using a denoising model trained with N2V (Fiji plugin)[51], complemented by Gaussian filtering to optimize noise reduction. Residual motion was addressed by calculating pixel shifts in time-series images and applying registration or drift correction methods, resulting in signal-enhanced 2D images.

Additionally, the SRRF algorithm[12] was used to enhance image resolution from stacks. Original and enhanced images were compared, with FRC maps validating the resolution improvement, using a fixed 1/7 threshold value[52]. All processing steps were performed with Fiji plugins. To summarize all this, a schematic flow-chart of the analysis process is shown in Supplementary information Fig. S1.

Imaging of cellular lipid vesicles

Lipids were labeled using 120 μL of 1.67 mM SF44[53,54] dye (SPARK Biopharma, Seoul, South Korea) diluted in DMSO, heated to body temperature, and administered via intraocular injection 30 minutes before imaging. The SF44 dye, with absorption at 445 nm and emission at 611 nm, enabled visualization of lipid vesicles, distinguishing them from other targets. Lipid area was calculated by analyzing the blue channel representing lipid droplets.

Alcoholic liver disease model

To assess the clinical relevance of our imaging setup, we simulated an alcoholic liver disease model in mice. This model, based on previous studies[47], enabled the observation of changes in hepatocytes, lipid vesicles, and mitochondria during ethanol ingestion. Three groups of eight mice (six to eight weeks old, 1:1 gender ratio) were fed varying amounts of ethanol (70%, Daejung Reagent Chemicals, CAS No: 64-17-5) via oral gavage. The first group received a single dose via oral gavage, another received three doses at 12 hour intervals[55]. The third group was fed a Lieber-DeCarli (LD) Diet[46] containing 36% ethanol for 2 weeks, followed by a single dose of EtOH via oral gavage to create a more severe injury. A control group was fed a non-ethanol diet with a maltose gavage[56]. Mice were imaged across multiple sessions under anesthesia. After each imaging session, the mice were sutured and given pain management with ketoprofen (5 mg/kg, diluted to 1 mg/mL concentration). The details of the EtOH-administered models are summarized in Table S1.

Mitochondrial transition state

Mitochondrial state analysis was conducted using the Mitometer, a MATLAB application[57]. To assess mitochondrial transitions, we examined the effects of a fission inhibitor. Mitochondrial shape was analyzed with the Mitochondrial Network Analysis workflow[58] in Fiji, which quantified parameters like average branch length, network size, and mitochondrial coverage area.

Fission inhibitor

Berberine (BBR), a traditional Chinese medicine, has antioxidant and anti-apoptotic properties, protecting mitochondrial function and mitophagy under oxidative stress. It reduces cytochrome *c* expression and improves mitochondrial dysfunction by enhancing membrane potential ($\Delta\Psi_m$) and ATP production.

Following Berberine (BBR) (Sigma-Aldrich, Cat. No: B3251) administration, a model mimicking alcohol-induced acute liver injury was established to assess BBR protective effects. Mice were divided into four groups: control, ethanol, and two BBR-treated groups. The control and ethanol groups received an equal volume of vehicle, while the BBR-treated groups were administered BBR at doses of 200 mg/kg/day and 300 mg/kg/day for 7 days. After treatment, the control group received saline[59,60] and other groups received three doses of ethanol (6 g/kg, every 12 hours).

In a separate experiment, we used a chronic ethanol feeding model combined with BBR treatment to investigate BBR's effects on mitochondrial fission. Mice were divided into in three groups and they were fed an isocaloric LD diet with either 0% or 36% ethanol for 2 weeks. The groups included Control, LD Diet, and LD Diet with BBR (120 mg/kg/day), the BBR dose was based on prior studies[46]. The control group received a liquid diet without ethanol, while the other two groups were given an LD Diet containing 36% ethanol following a single dose of ethanol[46,61]. The details of the BBR-treated models are summarized in Supplementary informationTable S2.

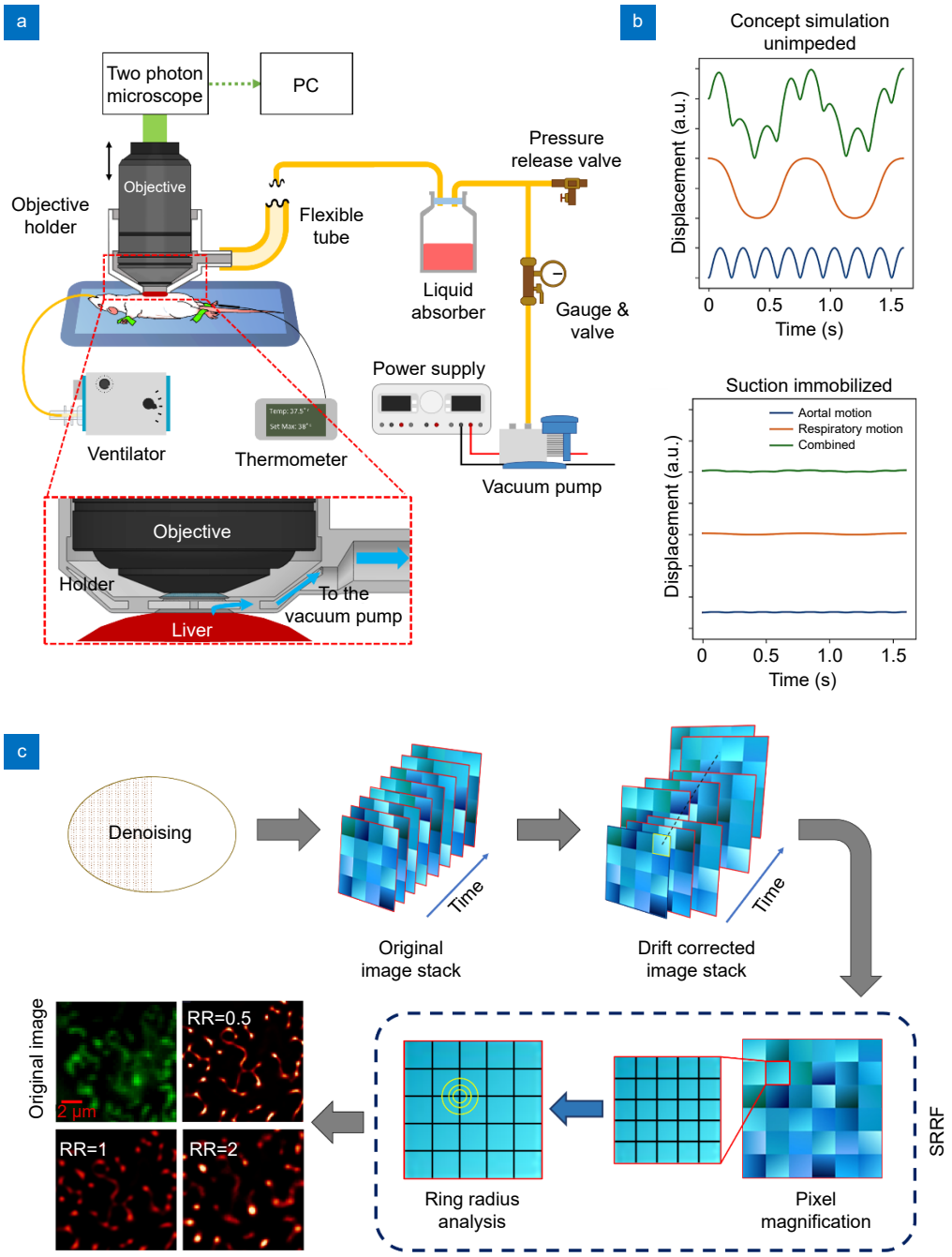

Fig. 1 | Schematic of suction-based stabilization for super-resolution radial fluctuations (SRRF) intravital imaging. (**a**) Schematic of intravital imaging setup with a suction-based stabilizer attached to the objective lens of a two-photon microscope. (**b**) Simulation of the expected stabilization effect on tissue displacement due to cardiac and respiratory motion. (**c**) Schematic of software drift correction and registration, followed by image postprocessing. Subsequent subpixel production and radiality analysis using the SRRF algorithm are depicted. (bottom left) Different ring radius values result in different effects on biological images.

H&E staining

The mice were sacrificed to obtain the primary organs for H&E staining. The organs were then fixed in a 4% paraformaldehyde solution for at least 24 h before being made into paraffin sections. Subsequently, they were H&E stained to visualize cellular morphology[62].

Immunofluorescence staining

Organs were harvested from animals, fixed in sucrose for 24 h, and processed into frozen blocks, which were sectioned into cryosections. For antigen retrieval, tissue slides were placed in 0.01 M sodium citrate solution, boiled for 3 minutes, and then incubated in a sodium

citrate Tween 20 solution for 1 hour at room temperature. After six washes with distilled water and PBS, the slides were incubated overnight at 4 °C with a 1:200 dilution of anti-GFP antibody (Abcam, UK , ab290 rabbit antibody). The next day, the slides were washed and incubated for 2 hours at room temperature with Alexa Fluor 555 goat anti-rabbit IgG (Abcam, UK) secondary antibody. Following additional washes, the slides were counterstained with 1:1000 diluted DAPI (Invitrogen, Waltham, Massachusetts, USA) for 5 minutes. After final washes, the slides were mounted and visualized using a confocal microscope (LSM880, Zeiss).

Results

A suction stabilization device was designed for intravital imaging, enabling long-term stack collection essential for computational resolution enhancement algorithms like SRRF to achieve nanoscale imaging of in vivo subcellular structures. It integrates previously established techniques not applied at this scale for intravital imaging. This device, as shown in Fig. 1(a), attaches to the objective lens, featuring a "wet" chamber with a transparent imaging window. Suction immobilizes tissue, enabling high numerical aperture use and reducing motion artifacts from cardiac and respiratory activity (Fig. 1(b)). Despite residual motion, lateral displacement was minimized and further corrected, as demonstrated in Fig. 1(c). Radiality analysis and optimization of the ring radius enhance the performance of the SRRF algorithm, resulting in improved resolution.

Device resolution

The device resolution was calibrated by imaging fluorescent micro-beads using conventional two-photon microscopy. The acquired data were then processed with the algorithm specified under "Image analysis" above, which includes denoising and image enhancement using the SRRF algorithm to achieve improved resolution and clarity. As shown in Fig. 2, conventional two-photon microscopy achieved resolutions between 0.5 μm and 1 μm,

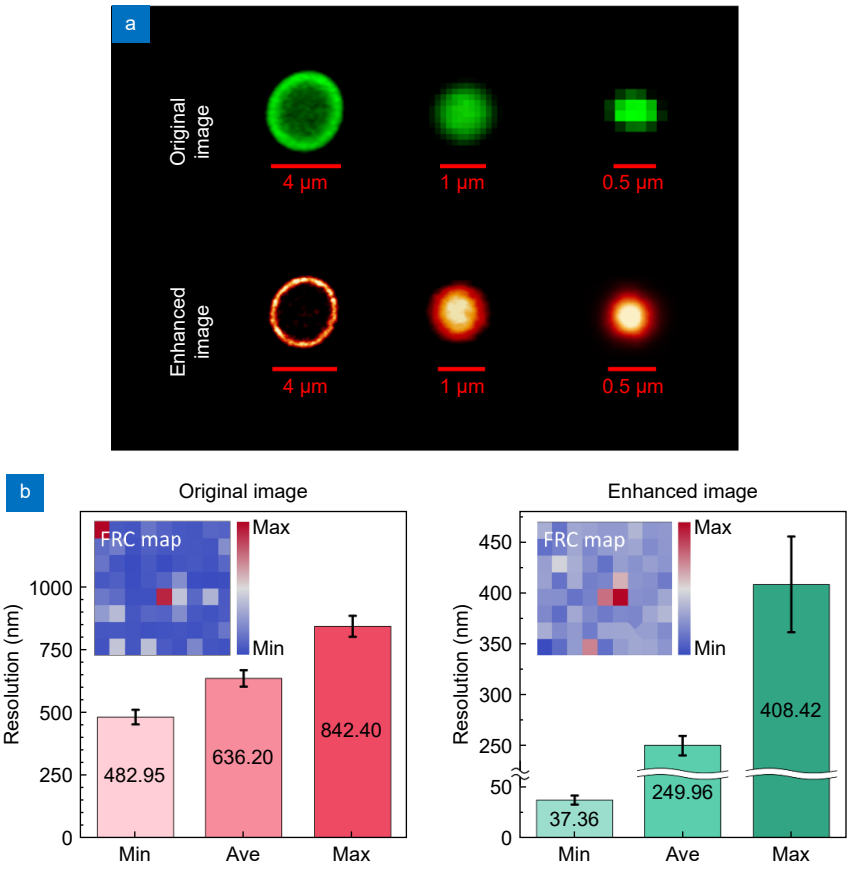

Fig. 2 | Comparisons between conventional two-photon and SRRF-assisted two-photon imaging. (**a**) SRRF imaging improves upon conventional two-photon imaging in the resolution of fine features when imaging fluorescent micro-beads. (**b**) FRC analysis comparing the resolution of conventional and enhanced tissue imaging demonstrates a significant improvement in SRRF resolution, averaging 250 nm. (Inset) FRC maps depict the image resolution in both the original and enhanced imaging of a fluorescent bead sample.

while SRRF-enhanced images approximately doubled the effective resolution. Fourier ring correlation (FRC) analyses[63,64] revealed average resolutions of 640 nm for conventional and 250 nm for SRRF-enhanced imaging. The worst resolution for SRRF images was still superior to the best conventional two-photon images. To further assess the imaging setup, the resolution of both the two-photon and SRRF pipelines was compared with a Airyscan confocal microscope using *ex vivo* mouse liver histology, as shown in Supplementary informationFig. S2.

Suction stabilization for *in vivo* imaging

The efficacy of the proposed method was experimentally evaluated through abdominal skin imaging. Epidermal imaging was achieved after preparation of the region, and suction stabilization showed clear effectiveness, as demonstrated in Supplementary Movie 1. Figure 3 provides example images of the abdominal skin, which is typically distorted by cardiac motion. In Fig. 3(a), images were captured at regular intervals, both with and without suction stabilization. As clearly illustrated by the red triangle and yellow circle markers, which indicate regions of interest (ROI), the unstabilized images not only exhibit fluctuations and movement of the ROI but also reveal changes in morphology due to motion in the *XYZ* directions. In contrast, the stabilized images demonstrate smooth, consistent imaging, with minimal movement and greater stability in both the field of view and

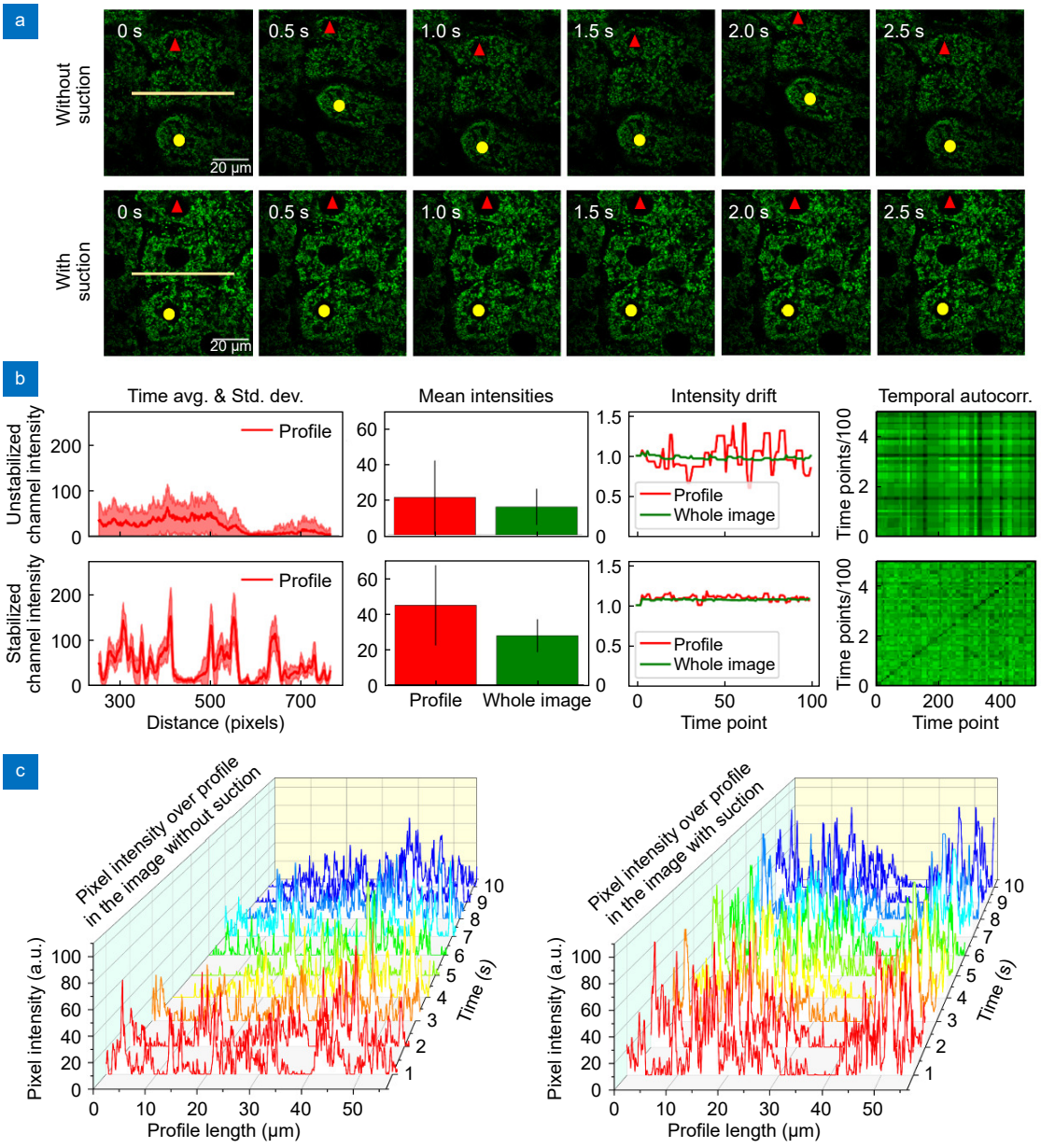

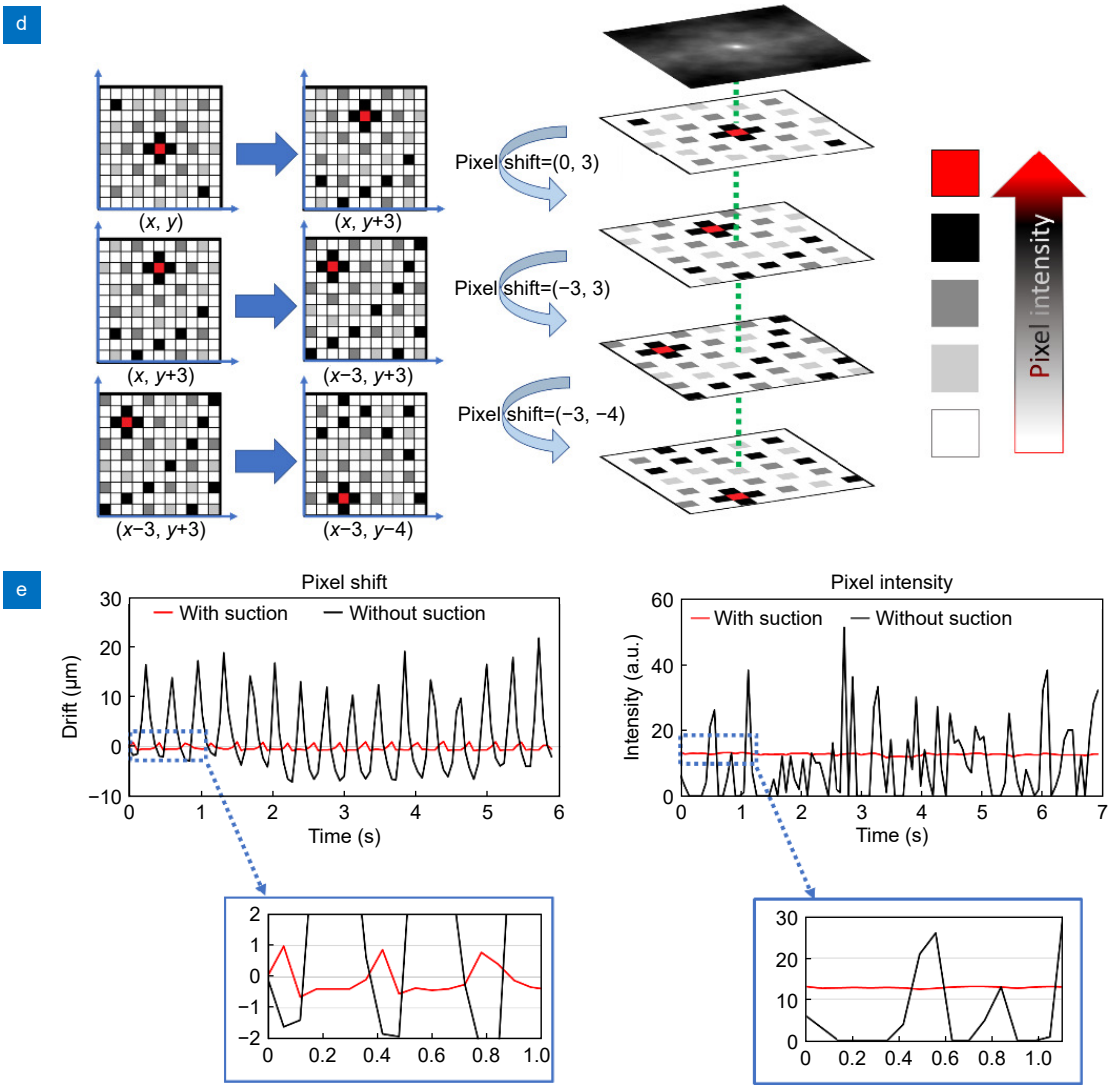

Fig. 3 | Suction stabilization was assessed using epidermal two-photon imaging of mito-Dendra2 mice. (**a**) Unstabilized (top) and stabilized (bottom) frames from a 2.5 s video show improved image consistency in the stabilized frames due to axial tissue stabilization, as indicated by the yellow lines in (**b**). Red triangles and yellow circles demonstrate movement of features of interest between frames. (**b**) Image intensity variance comparison reveals reduced variability in the stabilized stack, with more consistent temporal autocorrelation (i) along the highlighted profile, (ii) comparing the spatial average and intensity variance of the profile and full image, (iii) correlated intensity over the profile and whole-image changes more in the unstabilized image. (iv) Temporal correlations are more consistent in the stabilized image. (**c**) 3D projections highlight the stabilization effect in both hardware and software. (**d**) Schematic illustrates how suction reduces pixel shift and stabilizes pixel intensity. (**e**) Suction also minimizes pixel drift, stabilizing pixel intensity.

the tissue morphology. Figure 3(b) presents quantitative comparisons between imaging with and without stabilization, evaluating key parameters such as intensity, drift, and autocorrelation values to assess the impact of stabilization.

To quantitatively assess stabilization, we calculated the standard deviation of intensity, temporal drift, and autocorrelation for the full image and depicted profile (Fig. 3(c)). Drift was measured using the first frame as a reference (Fig. 3(d)), and drift and intensity plots for stabilized versus unstabilized images are shown in Fig. 3(e). Results indicated that stabilized image exhibited lower intensity deviations, reduced temporal drift, and more consistent autocorrelation[65]. Specifically, the mean temporal intensity standard deviation was 26.3 for unstabilized and 9.2 for stabilized profiles, improving the signal-to-noise ratio from 0.85 to 2.08. Additionally, the root mean square (RMS) deviation from the mean pixel shift

was 0.56 μm for stabilized images and 7.2 μm for unstabilized images, as shown in Fig. 3(e). Furthermore, the Pearson's correlation coefficient for the stabilized images was 0.90, indicating a high degree of similarity between consecutive frames, compared to 0.20 for the unstabilized images, highlighting the effectiveness of the stabilization process.

Image enhancement via SRRF in suction-stabilized two-photon microscopy

Tissue stabilization facilitated SRRF imaging by enabling the acquisition of nearly identical image sequences. SRRF-enhanced images of mouse skin demonstrated superior resolution, characterized by sharper intensity peaks in mitochondrial fluorescence compared to conventional two-photon stacks. These enhanced images exhibited increased intensity, improved signal-to-noise ratios, and finer structural details while maintaining the full field of view (Fig. 4(a)). Line profiles from enhanced images were consistently narrower, emphasizing enhanced feature sharpness (Fig. 4(b)). High-resolution images of the exteriorized murine liver were acquired at 15 fps using SRRF on image stacks. While capturing thousands of frames was feasible, it significantly increased motion artifacts and processing time. The raw liver image (Fig. 4(c)) and its magnified view (Fig. 4(d)) revealed intricate mitochondrial structures. SRRF enhanced image clarity, enabling clear distinction between cell nuclei and mitochondria. *Z*-scanning (Fig. 4(e)) and 3D rendering (Fig. 4(f)) provided detailed view of mitochondrial networks within hepatocytes.

Supplementary Movie 2 and 3 show 3D animations and time-lapse enhanced imaging, highlighting mitochondrial changes over time, with potential clinical relevance *in vivo*. Supplementary Fig. S3 shows that SRRF processing enhanced feature resolution, reducing the full width at half maximum from 1 μm in the original images to 300–600 nm in enhanced images. Figure S4 demonstrates that enhanced images of various organs (kidney, heart, brain, small intestine, colon, liver) closely resembled H&E-stained histology, offering higher resolution and enabling *in vivo* imaging prior to biopsy.

Demonstration of mitochondrial imaging in acute ethanol-induced liver injuries

We assessed the impact of ethanol on murine liver mitochondria and hepatocyte morphology in three groups of mice treated with berberine (Fig. 5). The control group received a standard diet, a vehicle solution, and three doses of PBS. The first treatment group received the vehicle followed by three ethanol doses (6 g/kg) at 12-hour intervals. The second and third groups were given berberine at different doses and three doses of ethanol, similar to the first group. Mitochondrial dynamics were monitored in real-time using enhanced SRRF imaging. In the control group, Dendra2-tagged mitochondria were elongated and interconnected, whereas ethanol treatment shortened and rounded them. Berberine (10 mg BBR, 300 mg/kg/day) restored mitochondrial length, which was reduced by 22% with ethanol, and normalized mitochondrial morphology[57], including roundness and solidity, to control levels (Fig. 5).

Imaging of the mito-Dendra2 mouse liver under ethanol and BBR treatment revealed significant gaps in the mitochondrial network, though the cause of these holes—whether from cell nuclei, lipids, vesicles, or gas bubbles—remained unclear.

Distinguishing nuclei from lipids with SF44 in liver mitochondrial morphology

To investigate the origin of voids in the mitochondrial network, intravital imaging using SF44[53], lipid stain was performed in a mouse model. It was hypothesized that these voids stem from hepatic lipid droplet accumulation. Mice were fed the Lieber–DeCarli (LD) diet[66] and divided into three groups: LD control, LD with ethanol (EtOH), and LD with EtOH plus berberine (BBR) treatment. Figure S5(a) shows a significant increase in lipid vesicle number and size in the ethanol and BBR-treated groups. SF44 staining distinguished lipid droplets from other cellular components, and intravital imaging confirmed lipid-filled vacuoles in hepatocytes.

Supplementary Fig. S5(b) shows the mean area, total area, and total number of lipid vesicles. The data indicate that ethanol and BBR treatment promoted droplet agglomeration, with vesicle size increasing and their number decreasing. This confirmed the formation of large lipid vesicles in hepatocytes. Notably, lipid droplet accumulation was also observed in the BBR group, despite its potential as a treatment for liver cirrhosis and alcoholic fatty liver disease.

Direct real-time observation of mitochondrial fission, fusion, and motion tracking

The *in vivo* tracking of mitochondrial dynamics is crucial for understanding mitochondrial pathologies. Using

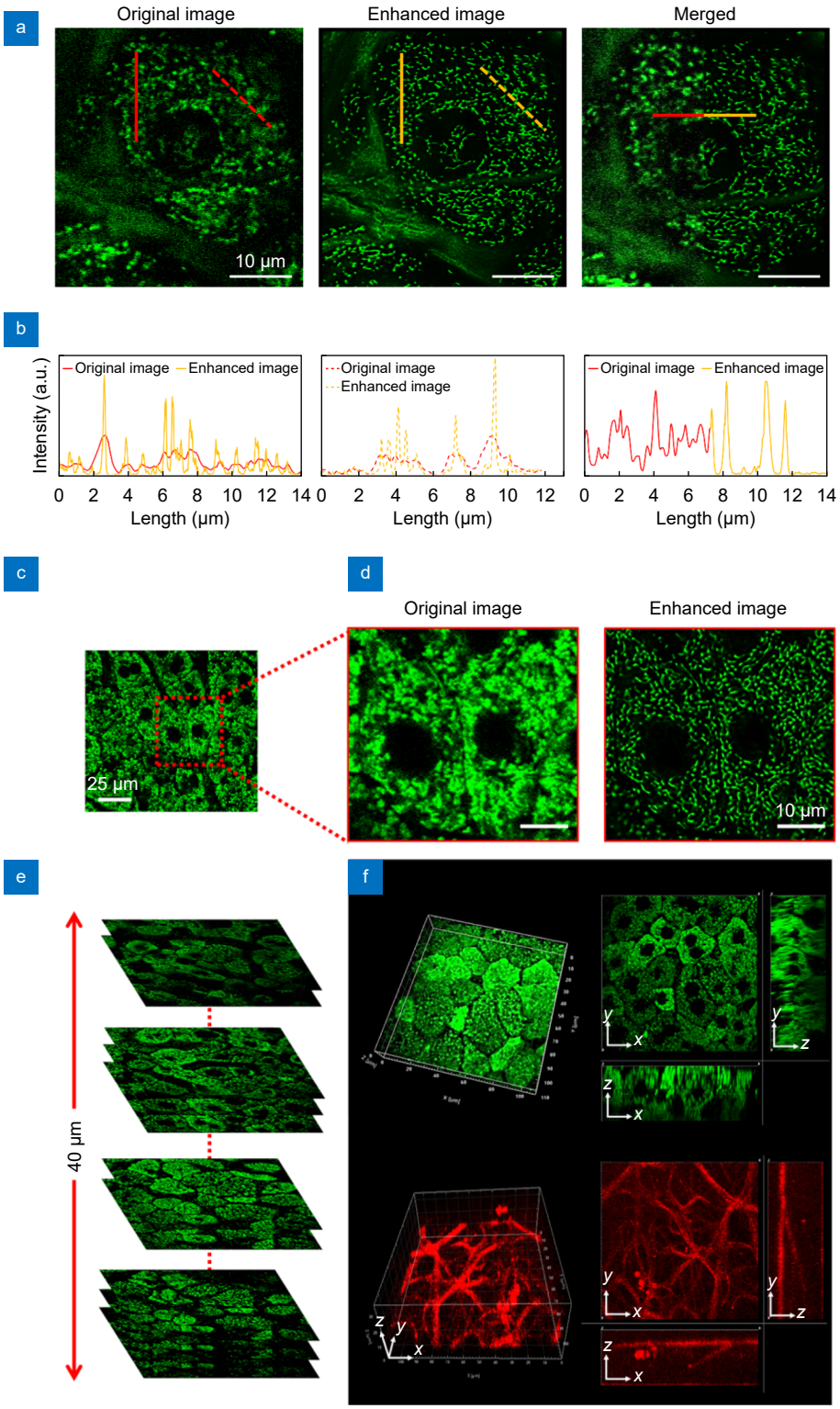

Fig. 4 | Intravital two-photon skin and liver imaging with suction stabilization. (**a**) Comparison between the original image (left, red line) and the enhanced version (middle, yellow line), with the merged image (right) displaying half of the original image overlaid with the enhanced image for direct visual contrast. (**b**) Pixel intensities shown along the solid and dashed profiles, revealing sharper image features in the enhanced image. (**c**) Demonstrate original hepatocyte imaging. (**d**) Hepatocyte imaging with denoising, image registration, and SRRF. Scale bar, 10 μm. (**e**) Schematic of *z*-scan enhanced imaging enabled by image stabilization, showing image stacks at depths from 40 μm. (**f**) 3D visualizations of the enhanced image *z*-stack. The upper row shows the hepatocytes and the lower one demonstrates the blood vessels tagged by Texas red dextran.

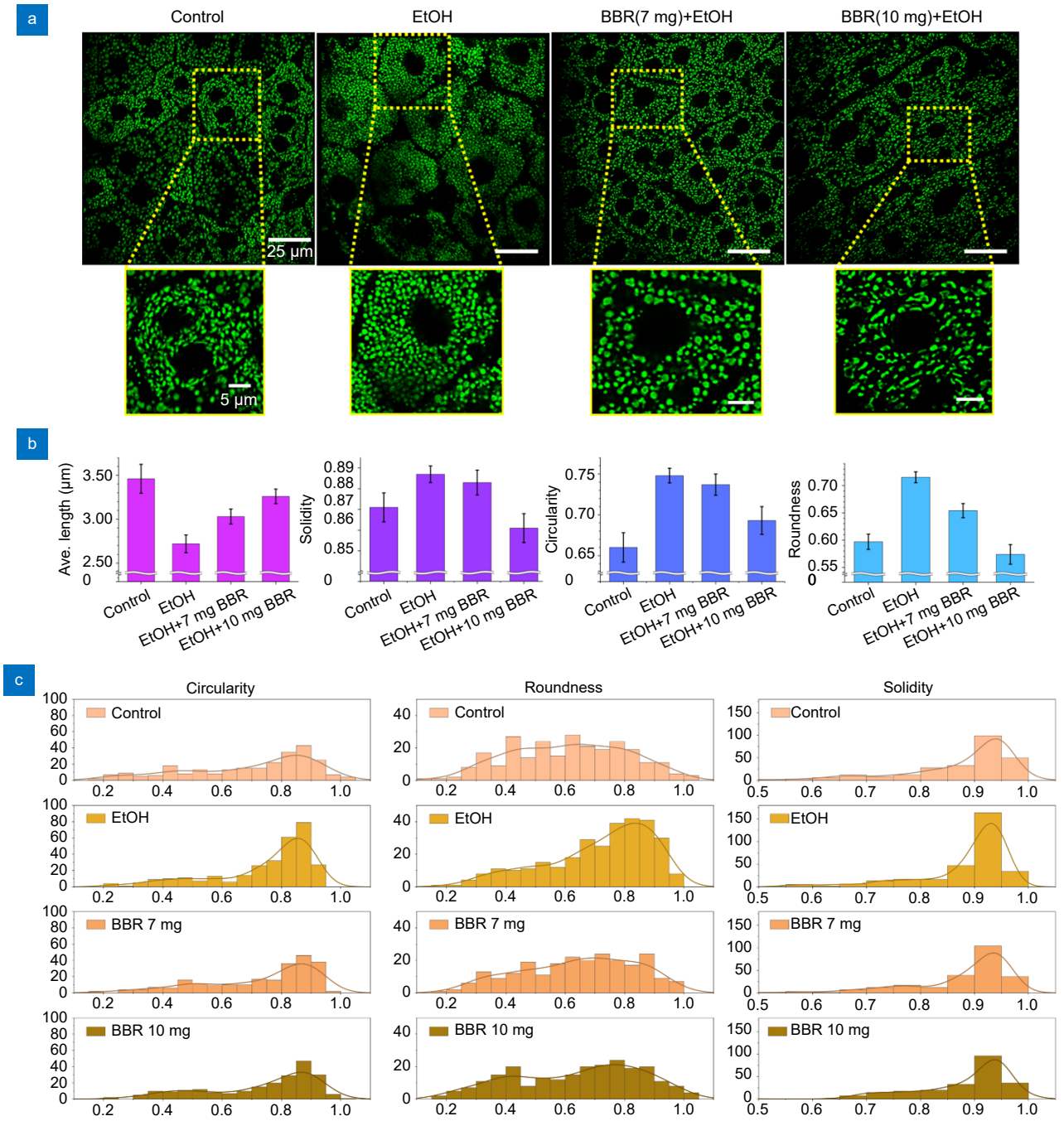

Fig. 5 | Effects of ethanol (EtOH) and berberine (BBR) treatment on the mitochondrial network in the exteriorized mouse liver. (**a**) Two-photon enhanced images from the mouse liver show changes in mitochondrial morphology under treatment with ethanol and different concentrations of BBR. (**b**) From left to right: mitochondrial length, solidity, circularity, and roundness, as calculated from enhanced images. The average mitochondrial length is reduced by ethanol and restored by treatment with BBR. (**c**) Histograms showing the distribution of mitochondria with different values of circularity, roundness, and solidity, for the control, ethanol treatment, and treatment with doses of 7 and 10 mg BBR. *P* values are determined using two-tailed *t*-test. **P* < 0.05, ***P* < 0.01, ****P* < 0.001, *****P* < 0.0001.

suction stabilization, time-lapse SRRF enhanced imaging employed to capture mitochondrial behavior in the mouse liver. Figure 6(a) shows steady-state images of untreated liver mitochondria, highlighting their varying connectivity, with fused mitochondria appearing long and string-like, and fissioned ones being short and round. Fusion and fission events were observed simultaneously in the same field (Fig. 6(b)), with arrows marking fusion and arrowheads indicating fission. This setup enabled stable and high-resolution imaging over extended

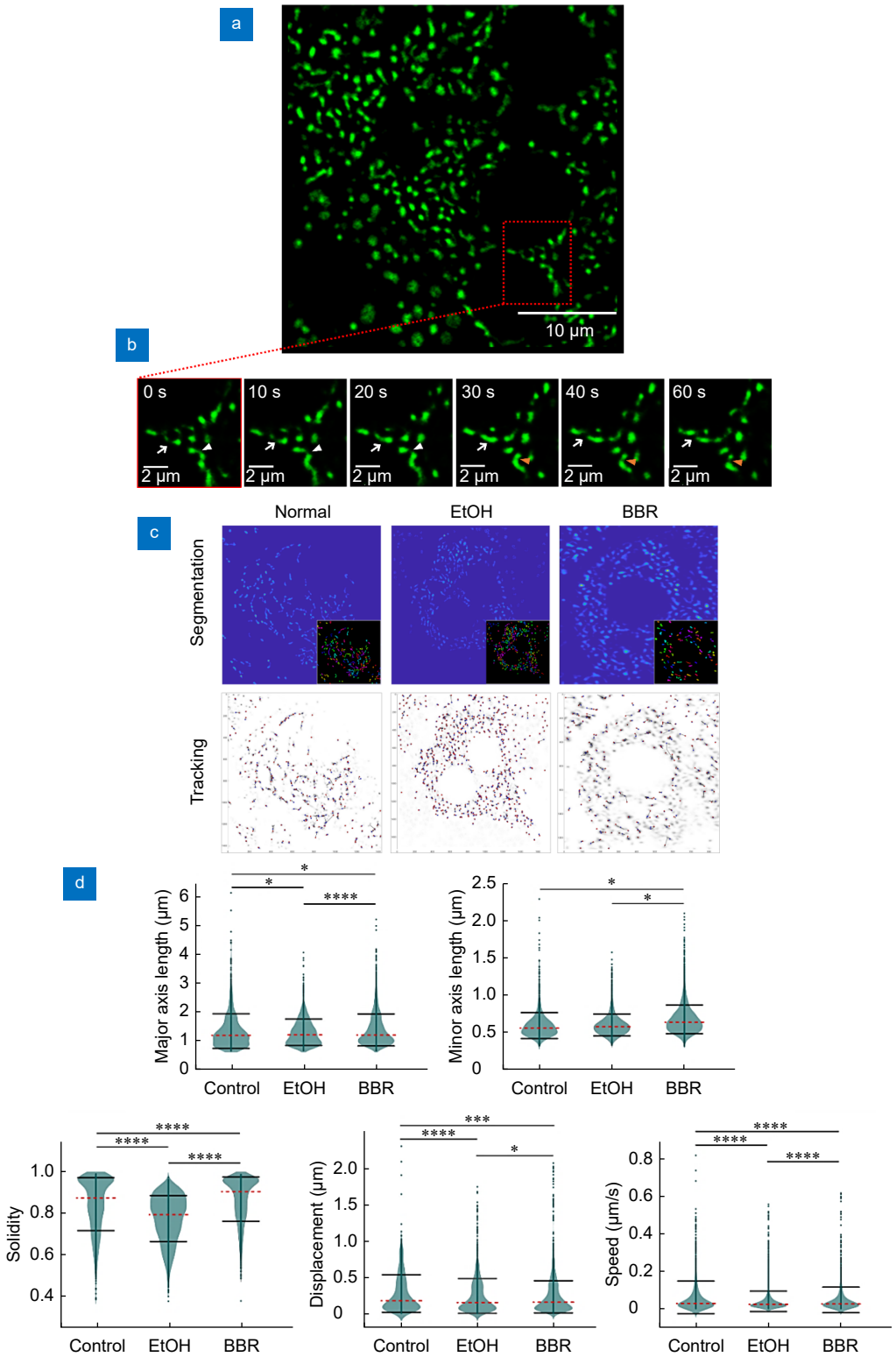

Fig. 6 | Live intravital tracking of mitochondrial transitions using suction-stabilized two-photon imaging with SRRF. (**a**) Contextual image showing an optical liver section from an untreated mouse. (**b**) Intravital time-lapse fission and fusion of individual mitochondria. (Arrows) fusion; (arrowheads) fission. (**c**) Segmentation and tracking of mitochondrial migration in control, EtOH-fed, and BBR-treated groups with randomly labeled objects in the lower corner (first row) and tracking mitochondria (second row). (**d**) Major and minor axis, solidity, displacement, and speed of individual mitochondria in three different groups of mice. *P* values are determined using two-tailed *t*-test. **P* < 0.05, ***P* < 0.01, ****P* < 0.001, *****P* < 0.0001.

periods.

To automate mitochondrial tracking, we used the Mitometer framework by Lefebvre et al.[67] to analyze control, ethanol-fed (EtOH), and berberine-treated (BBR) mice over a 10 second interval. Segmented SRRF images (Fig. 6(c)) allowed tracking of individual mitochondria, depicted as randomly labeled objects. Comparative analysis revealed significant differences in mitochondrial morphology and mobility, including axis lengths, displacement, solidity, and speed (Fig. 6(d)). Control and BBR-treated mice showed elongated mitochondria, indicating less circular morphology and reduced fission, while EtOH-fed mice exhibited lower speed and displacement, reflecting diminished energy and dynamics.

Supplementary informationFig. S6 and Movie 4 showcase mitochondrial transitions, revealing individual fission and fusion events. Over longer timescales, dynamic waves of high-fusion and high-fission regions traverse the 110-micron field of view.

These findings highlight altered metabolism, mitochondrial dysfunction, and cellular stress in alcohol-damaged hepatocytes, offering insights into mitochondrial displacement and mobility in these pathological states.

Discussion

We developed an optical setup enabling *in vivo* super-resolution imaging using two-photon microscopy at sub-micron scale resolution providing physiologically relevant images[68,69]. Suction-based passive stabilization, used at 25 mmHg, minimized invasiveness, preserved blood circulation, and limited tissue damage, remaining effective without visible damage up to 100 mmHg, below typical mouse blood pressure[70]. Previous research has also indicated that suction devices have negligible effects on perfusion[71] at pressures of 75 mmHg, although a slight suppressive effect has been observed[72]. This reduced cardiac motion artifacts from hundreds of pixels to under 10, surpassing previous methods[32] that relied on active modulation or image gating. Computational frame registration further enhanced precision while maintaining tissue integrity.

Compared to earlier approaches[29,32–34,73], our device integrates seamlessly with the microscope objective or can be free-mounted above the tissue, allowing for prolonged experiments and subcellular feature tracking with minimal tissue disruption. This enables continuous observation of disease progression and treatment effects *in vivo*.

Using the SRRF technique, we captured super-resolution images of mitochondrial dynamics during alcohol-induced liver disease and treatment with a mitochondrial fission inhibitor. While both suction and SRRF have been employed separately in several investigations, their combined use for sub-micron scale intravital imaging and 3D reconstruction of mitochondrial networks is unprecedented. This approach facilitates rapid, repeated, and extended time-lapse imaging without the limitations of fluorophore bleaching or structured illumination used by super-resolution techniques.

We investigated the impact of alcohol and berberine (BBR) treatment on hepatic lipid vesicles (Supplementary Fig. S5). Lipids play a crucial role in ethanol-induced liver injury due to their involvement in ethanol metabolism. Ethanol is primarily metabolized[74] in the liver via two pathways: the alcohol dehydrogenase (ADH) pathway[75], which converts ethanol to the toxic acetaldehyde, and the microsomal ethanol oxidizing system (MEOS) pathway[76], which generates reactive oxygen species (ROS)[77]. Chronic alcohol consumption enhances the MEOS pathway, leading to ROS accumulation and lipid peroxidation. This process damages liver cells and contributes to steatosis, marked by fat accumulation as lipid droplets. Thus, lipid accumulation is a critical indicator of ethanol-induced liver damage mediated by ROS and lipid peroxidation.

We observed lipid droplet accumulation and potential agglomeration in mouse livers following an alcohol-containing diet, undetectable by conventional imaging. This effect was exacerbated by berberine (BBR) treatment, a potential therapy for liver cirrhosis and alcoholic fatty liver disease[78]. In the alcohol-fed group, lipid droplet size increased while count decreased. BBR treatment further enlarged vesicles and reduced droplet numbers, suggesting either a therapeutic mechanism or a side effect.

Lipid droplet size reflects cellular metabolic status, indicating increased energy storage capacity and potential cellular stress. These droplets interact with mitochondria and the endoplasmic reticulum, linking their size changes to shifts in energy metabolism and cellular processes.

We investigated berberine's (BBR) protective effects on liver mitochondria under alcohol-induced stress. Binge drinking reduced mitochondrial length by 22%, while BBR pretreatment (10 mg, 300 mg/kg/day) restored it near control levels. Beyond its known role in

enhancing mitochondrial function by boosting respiration and ATP production[79,80], our study reveals BBR's influence on mitochondrial morphology. BBR treatment also increased antioxidant enzyme activity and reduced mitochondrial ROS, mitigating oxidative stress and lowering the mitochondrial fission, with stronger effects at higher doses (Fig. 5(b)).

We observed that suction increased blood flow rate in vessels, independent of vessel diameter. While negative pressure treatments can therapeutically enhance blood flow[72], the risk of capillary rupture must be considered. Comparing conditions without suction, slight pressure from a slide glass, and suction (Supplementary Fig S7, Supplementary Movie 5), no capillary ruptures were observed, although capillary dilation was not specifically examined. Additionally, to ensure that the SRRF algorithm does not alter the morphology of the target, we captured images of microbeads and stained tissue paper before and after applying SRRF for comparison. These references provide a structural benchmark to verify that the algorithm preserves the original morphology (Supplementary Fig. S8). Similar work has been done by Culley et al. to show the fidelity of SRRF to both diffraction-limited fluorescence microscopy[52] and to physical super-resolution fluorescence methods like dSTORM[12].

Suction stabilization, while effective for reducing motion artifacts, carries a risk of tissue damage[81]. During prolonged imaging sessions (e.g., 3 hours), issues such as blood accumulation near the imaging site and tissue surface drying were noted but mitigated with periodic PBS application. Although blood redistribution occurred post-imaging and no damage was observed in our sessions, extended imaging may still pose a risk of localized ischemia, as tissue color normalized once suction was discontinued. Additionally, to ensure the accuracy and reliability of our proposed method to estimate the impact of negative pressure on cellular morphology, we conducted an experiment to analyze lipid size in the exposed liver, both with and without suction. This analysis provided valuable insights into the effects of suction on lipid morphology, further reinforcing the validity of our findings (Supplementary Fig. S9).

The suction stabilization method combined with the SRRF algorithm offers versatile applications, from intravital imaging in mice to other animal models and potential clinical use. This approach enables organelle-level mechanistic studies and drug evaluations *in vivo*, adaptable to various microscopes and imaging techniques, including structured illumination and fluorescence lifetime imaging. Notably, the device's attachment to objective lenses improves compatibility, expanding its use across various imaging systems.

Conclusion

In conclusion, we integrated super-resolution techniques with two-photon microscopy for intravital imaging of GFP-labeled mitochondria in live mice. This stabilization method enables a clear real-time observation of mitochondrial transitions, addressing challenges in imaging dynamic organelles *in vivo*. Our findings highlight the potential of super-resolution imaging to advance mitochondrial research by revealing subcellular processes in their native context.

References

1. Hoole S. *The Select Works of Antony Van Leeuwenhoek* (Henry Fry, London, 1798).
2. Pittet MJ, Weissleder R. Intravital imaging. *Cell* **147**, 983–991 (2011).
3. Saxena M, Eluru G, Gorthi SS. Structured illumination microscopy. *Adv Opt Photon* **7**, 241–275 (2015).
4. Scheele CLGJ, Herrmann D, Yamashita E et al. Multiphoton intravital microscopy of rodents. *Nat Rev Methods Primers* **2**, 89 (2022).
5. Denk W, Strickler JH, Webb WW. Two-photon laser scanning fluorescence microscopy. *Science* **248**, 73–76 (1990).
6. Hong H, Wu CC, Zhao ZX et al. Giant enhancement of optical nonlinearity in two-dimensional materials by multiphoton-excitation resonance energy transfer from quantum dots. *Nat Photon* **15**, 510–515 (2021).
7. Xia F, Wu CY, Sinefeld D et al. *In vivo* label-free confocal imaging of the deep mouse brain with long-wavelength illumination. *Biomed Opt Express* **9**, 6545–6555 (2018).
8. Xu X, Luo Q, Wang JX et al. Large-field objective lens for multi-wavelength microscopy at mesoscale and submicron resolution. *Opto-Electron Adv* **7**, 230212 (2024).
9. Liu S, Hoess P, Ries J. Super-resolution microscopy for structural cell biology. *Annu Rev Biophys* **51**, 301–326 (2022).
10. Huang YR, Zhang ZM, Tao WL et al. Multiplexed stimulated emission depletion nanoscopy (mSTED) for 5-color live-cell long-term imaging of organelle interactome. *Opto-Electron Adv* **7**, 240035 (2024).
11. Bon P, Linarès-Loyez J, Feyeux M et al. Self-interference 3D super-resolution microscopy for deep tissue investigations. *Nat Methods* **15**, 449–454 (2018).
12. Culley S, Tosheva KL, Pereira PM et al. SRRF: universal live-cell super-resolution microscopy. *Int J Biochem Cell Biol* **101**, 74–79 (2018).
13. Gustafsson N, Culley S, Ashdown G et al. Fast live-cell conventional fluorophore nanoscopy with ImageJ through super-resolution radial fluctuations. *Nat Commun* **7**, 12471 (2016).
14. Laine RF, Tosheva KL, Gustafsson N et al. NanoJ: a high-performance open-source super-resolution microscopy toolbox. *J Phys D: Appl Phys* **52**, 163001 (2019).
15. Bond C, Santiago-Ruiz AN, Tang Q et al. Technological advances in super-resolution microscopy to study cellular process-

es. *Mol Cell* **82**, 315–332 (2022).
16. Nguyen HTT, Kang SH. Base pair distance in single‐DNA molecule via TIRF‐based super‐resolution radial fluctuations‐stream module. *Bull Korean Chem Soc* **41**, 476–479 (2020).
17. Lee YH, Zhang S, Mitchell CK et al. Calcium imaging with super-resolution radial fluctuations. *Biosci Bioeng* **4**, 78–84 (2018).
18. Zhang JB, Li N, Dong FH et al. Ultrasound microvascular imaging based on super‐resolution radial fluctuations. *J Ultrasound Med* **39**, 1507–1516 (2020).
19. Stubb A, Laine RF, Miihkinen M et al. Fluctuation-based super-resolution traction force microscopy. *Nano Lett* **20**, 2230–2245 (2020).
20. Soulet D, Lamontagne‐Proulx J, Aubé B et al. Multiphoton intravital microscopy in small animals: motion artefact challenges and technical solutions. *J Microsc* **278**, 3–17 (2020).
21. Vinegoni C, Lee S, Aguirre AD et al. New techniques for motion-artifact-free in vivo cardiac microscopy. *Front Physiol* **6**, 147 (2015).
22. Warren SC, Nobis M, Magenau A et al. Removing physiological motion from intravital and clinical functional imaging data. *eLife* **7**, e35800 (2018).
23. Lee S, Nakamura Y, Yamane K et al. Image stabilization for *in vivo* microscopy by high-speed visual feedback control. *IEEE Trans Robot* **24**, 45–54 (2008).
24. Lee S, Ozaki T, Nakamura Y. In vivo microscope image stabilization through 3-D motion compensation using a contact-type sensor. In *2008 IEEE/RSJ International Conference on Intelligent Robots and Systems* 1192–1197 (IEEE, 2008). http://doi.org/10.1109/IROS.2008.4651123.
25. Vinegoni C, Lee S, Feruglio PF et al. Advanced motion compensation methods for intravital optical microscopy. *IEEE J Sel Top Quantum Electron* **20**, 6800709 (2014).
26. Reichenspurner H, Detter C, Deuse T et al. Video and robotic-assisted minimally invasive mitral valve surgery: a comparison of the Port-Access and transthoracic clamp techniques. *Ann Thorac Surg* **79**, 485–490 (2005).
27. Lee S, Vinegoni C, Feruglio PF et al. Real-time in vivo imaging of the beating mouse heart at microscopic resolution. *Nat Commun* **3**, 1054 (2012).
28. Aguirre AD, Vinegoni C, Sebas M et al. Intravital imaging of cardiac function at the single-cell level. *Proc Natl Acad Sci USA* **111**, 11257–11262 (2014).
29. Vinegoni C, Lee S, Gorbatov R et al. Motion compensation using a suctioning stabilizer for intravital microscopy. *Intravital* **1**, 115–121 (2012).
30. Kim Y, Cho M, Paulson B et al. Minimizing motion artifacts in intravital microscopy using the sedative effect of dexmedetomidine. *Microsc Microanal* **28**, 1679–1686 (2022).
31. Kiryu S, Sundaram T, Kubo S et al. MRI assessment of lung parenchymal motion in normal mice and transgenic mice with sickle cell disease. *J Magn Reson Imaging* **27**, 49–56 (2008).
32. Presson RG Jr, Brown MB, Fisher AJ et al. Two-photon imaging within the murine thorax without respiratory and cardiac motion artifact. *Am J Pathol* **179**, 75–82 (2011).
33. Terry RJ. A thoracic window for observation of the lung in a living animal. *Science* **90**, 43–44 (1939).
34. Looney MR, Thornton EE, Sen D et al. Stabilized imaging of immune surveillance in the mouse lung. *Nat Methods* **8**, 91–96 (2011).
35. Kim JK, Lee WM, Kim P et al. Fabrication and operation of GRIN probes for in vivo fluorescence cellular imaging of internal organs in small animals. *Nat Protoc* **7**, 1456–1469 (2012).
36. Rodriguez-Tirado C, Kitamura T, Kato Y et al. Long-term high-resolution intravital microscopy in the lung with a vacuum stabilized imaging window. *J Vis Exp* **116**, 54603 (2016).
37. Schrepfer E, Scorrano L. Mitofusins, from mitochondria to metabolism. *Mol Cell* **61**, 683–694 (2016).
38. Youle RJ, Van Der Bliek AM. Mitochondrial fission, fusion, and stress. *Science* **337**, 1062–1065 (2012).
39. van der Bliek AM, Shen QF, Kawajiri S. Mechanisms of mitochondrial fission and fusion. *Cold Spring Harb Perspect Biol* **5**, a011072 (2013).
40. Song ZY, Ghochani M, McCaffery JM et al. Mitofusins and OPA1 mediate sequential steps in mitochondrial membrane fusion. *Mol Biol Cell* **20**, 3525–3532 (2009).
41. López-Lluch G. Mitochondrial activity and dynamics changes regarding metabolism in ageing and obesity. *Mech Ageing Dev* **162**, 108–121 (2017).
42. Jheng HF, Tsai PJ, Guo SM et al. Mitochondrial fission contributes to mitochondrial dysfunction and insulin resistance in skeletal muscle. *Mol Cell Biol* **32**, 309–319 (2012).
43. Duraisamy AJ, Mohammad G, Kowluru RA. Mitochondrial fusion and maintenance of mitochondrial homeostasis in diabetic retinopathy. *Biochim Biophys Acta (BBA)-Mol Basis Dis* **1865**, 1617–1626 (2019).
44. Babayeva A. Změny mitochondriálního metabolismu u nádorových buněk (2023).
45. Cederbaum AI, Lu YK, Wu DF. Role of oxidative stress in alcohol-induced liver injury. *Arch Toxicol* **83**, 519–548 (2009).
46. Guo FF, Zheng K, Benedé‐Ubieto R et al. The Lieber‐DeCarli Diet—a flagship model for experimental alcoholic liver disease. *Alcohol Clin Exp Res* **42**, 1828–1840 (2018).
47. Ghosh Dastidar S, Warner JB, Warner DR et al. Rodent models of alcoholic liver disease: role of binge ethanol administration. *Biomolecules* **8**, 3 (2018).
48. Tillhon M, Ortiz LMG, Lombardi P et al. Berberine: new perspectives for old remedies. *Biochem Pharmacol* **84**, 1260–1267 (2012).
49. Yan XJ, Yu X, Wang XP et al. Mitochondria play an important role in the cell proliferation suppressing activity of berberine. *Sci Rep* **7**, 41712 (2017).
50. Schindelin J, Arganda-Carreras I, Frise E et al. Fiji: an open-source platform for biological-image analysis. *Nat Methods* **9**, 676–682 (2012).
51. Mannam V, Zhang YD, Zhu YH et al. Real-time image denoising of mixed Poisson–Gaussian noise in fluorescence microscopy images using ImageJ. *Optica* **9**, 335–345 (2022).
52. Culley S, Albrecht D, Jacobs C et al. Quantitative mapping and minimization of super-resolution optical imaging artifacts. *Nat Methods* **15**, 263–266 (2018).
53. Kim E, Lee S, Park SB. A Seoul-Fluor-based bioprobe for lipid droplets and its application in image-based high throughput screening. *Chem Commun* **48**, 2331–2333 (2012).
54. Lee Y, Na S, Lee S et al. Optimization of Seoul-Fluor-based lipid droplet bioprobes and their application in microalgae for bio-fuel study. *Mol BioSyst* **9**, 952–956 (2013).
55. Kirpich I, Ghare S, Zhang J W et al. Binge alcohol–induced microvesicular liver steatosis and injury are associated with down‐regulation of hepatic *Hdac 1, 7, 9, 10, 11* and up‐regulation of *Hdac 3*. *Alcohol Clin Exp Res* **36**, 1578–1586 (2012).
56. Bertola A, Mathews S, Ki SH et al. Mouse model of chronic and binge ethanol feeding (the NIAAA model). *Nat Protoc* **8**, 627–637 (2013).
57. Lefebvre AEYT, Ma D, Kessenbrock K et al. Author correction: automated segmentation and tracking of mitochondria in live-cell time-lapse images. *Nat Methods* **19**, 770 (2022).
58. Valente AJ, Maddalena LA, Robb EL et al. A simple ImageJ

macro tool for analyzing mitochondrial network morphology in mammalian cell culture. *Acta Histochem* **119**, 315–326 (2017).
59. Zhang PC, Ma DS, Wang YC et al. Berberine protects liver from ethanol-induced oxidative stress and steatosis in mice. *Food Chem Toxicol* **74**, 225–232 (2014).
60. Xu LL, Zheng X, Wang YH et al. Berberine protects acute liver failure in mice through inhibiting inflammation and mitochondria-dependent apoptosis. *Eur J Pharmacol* **819**, 161–168 (2018).
61. Zhou R, Lin JJ, Wu DF. Sulforaphane induces Nrf2 and protects against CYP2E1-dependent binge alcohol-induced liver steatosis. *Biochim Biophys Acta (BBA)-Gen Subj* **1840**, 209–218 (2014).
62. Feldman AT, Wolfe D. Tissue processing and hematoxylin and eosin staining. *Methods Mol Biol* **1180**, 31–43 (2014).
63. Banterle N, Bui KH, Lemke EA et al. Fourier ring correlation as a resolution criterion for super-resolution microscopy. *J Struct Biol* **183**, 363–367 (2013).
64. Koho S, Tortarolo G, Castello M et al. Fourier ring correlation simplifies image restoration in fluorescence microscopy. *Nat Commun* **10**, 3103 (2019).
65. Woolrich MW, Ripley BD, Brady M et al. Temporal autocorrelation in univariate linear modeling of FMRI data. *Neuroimage* **14**, 1370–1386 (2001).
66. Lieber CS, DeCarli LM. Liquid diet technique of ethanol administration: 1989 update. *Alcohol Alcohol* **24**, 197–211 (1989).
67. Lefebvre AEYT, Ma D, Kessenbrock K et al. Automated segmentation and tracking of mitochondria in live-cell time-lapse images. *Nat Methods* **18**, 1091–1102 (2021).
68. Carvalho JCO, Palero JA, Jurna M. Real-time imaging of suction blistering in human skin using optical coherence tomography. *Biomed Opt Express* **6**, 4790–4795 (2015).
69. Shimizu K, Higuchi Y, Kozu Y et al. Development of a suction device for stabilizing *in vivo* real-time imaging of murine tissues. *J Biosci Bioeng* **112**, 508–510 (2011).
70. Uechi M, Asai K, Osaka M et al. Depressed heart rate variability and arterial baroreflex in conscious transgenic mice with overexpression of cardiac Gsα. *Circ Res* **82**, 416–423 (1998).
71. Wackenfors A, Sjögren J, Gustafsson R et al. Effects of vacuum‐assisted closure therapy on inguinal wound edge microvascular blood flow. *Wound Repair Regener* **12**, 600–606 (2004).
72. Smyth CN. Effect of suction on blood-flow in ischæmic limbs. *Lancet* **294**, 657–659 (1969).
73. Paulson B, Darian SB, Kim Y et al. Spectral multiplexing of fluorescent endoscopy for simultaneous imaging with multiple fluorophores and multiple fields of view. *Biosensors* **13**, 33 (2022).
74. You M, Arteel GE. Effect of ethanol on lipid metabolism. *J Hepatol* **70**, 237–248 (2019).
75. Tilg H, Moschen AR, Kaneider NC. Pathways of liver injury in alcoholic liver disease. *J Hepatol* **55**, 1159–1161 (2011).
76. Lieber CS, Rubin E, DeCarli LM. Hepatic microsomal ethanol oxidizing system (MEOS): differentiation from alcohol dehydrogenase and NADPH oxidase. *Biochem Biophys Res Commun* **40**, 858–865 (1970).
77. Jaeschke H. Reactive oxygen and mechanisms of inflammatory liver injury: present concepts. *J Gastroenterol Hepatol* **26**, 173–179 (2011).
78. Ke XM, Zhang RY, Li P et al. Hydrochloride Berberine ameliorates alcohol-induced liver injury by regulating inflammation and lipid metabolism. *Biochem Biophys Res Commun* **610**, 49–55 (2022).
79. Hori I, Harashima H, Yamada Y. Development of a mitochondrial targeting lipid nanoparticle encapsulating berberine. *Int J Mol Sci* **24**, 903 (2023).
80. Yu WL, Sheng MW, Xu RB et al. Berberine protects human renal proximal tubular cells from hypoxia/reoxygenation injury via inhibiting endoplasmic reticulum and mitochondrial stress pathways. *J Transl Med* **11**, 24 (2013).
81. Rosen M, Hillard EK. The use of suction in clinical medicine. *Br J Anaesth* **32**, 486–504 (1960).

Acknowledgements

This study was supported by the Ministry of Science, ICT and Future Planning (MSIP) through the National Research Foundation of Korea (NRF) (RS-2024-00450201), also supported by a grant from the Korea Health Technology R&D Project through the Korea Health Industry Development Institute (KHIDI), funded by the Ministry of Health and Welfare, Republic of Korea (HI22C1374).

Author contributions

Conceptualization, J.K.K.; methodology, J.K.K., S.B.D.; 3D holder design, S.B.D.; animal experiments, S.B.D., J.O., M.G., M.J.; data curation and image processing, S.B.D.; resource and analyses, S.B.D, G.K., E.T., I.K., C.G.P., J.M.N., and I.J.B.; writing—original draft preparation, S.B.D., J.O., I.J.B. and B.P.; writing—review and editing, all authors; visualization, S.B.D., B.P.; supervision, J.K.K.; funding acquisition, J.M.N. and J.K.K. All authors have read and agreed to the published version of the manuscript.

Competing interests

The authors declare no conflict of interest. The funders had no role in the design of the study; in the collection, analyses, or interpretation of data; in the writing of the manuscript; or in the decision to publish the results.

Ethical statement

The animal study protocol was approved by the Animal Care and Use Committee of Asan Medical Center (protocol 2021-12-030, approved 10 February 2021).

Data Availability

The data used in this study are openly available in repository at Zenodo at the following link:
https://doi.org/10.5281/zenodo.15080631

Supplementary information

Supplementary information for this paper is available at
https://doi.org/10.29026/oea.2025.240311

Scan for Article PDF